



The effect of dislocations on the efficiency of InGaN/GaN solar cells



Y. Zhang^{a,*}, M.J. Kappers^a, D. Zhu^a, F. Oehler^a, F. Gao^b, C.J. Humphreys^a

^a Department of Materials Science and Metallurgy, University of Cambridge, Cambridge CB2 3QZ, UK

^b Department of Physics, Cavendish Laboratory, University of Cambridge, Cambridge CB3 0HE, UK

ARTICLE INFO

Article history:

Received 3 February 2013

Received in revised form

22 May 2013

Accepted 14 June 2013

Available online 9 July 2013

Keywords:

GaN

InGaN

TEM characterization

EQE

Defects

ABSTRACT

Two solar cells based on an InGaN/GaN *p-i-n* hetero-junction, but having different dislocation densities, were fabricated and characterized. The structures were grown on *c*-plane (0001) GaN-on-sapphire templates with different threading dislocation (TD) densities of 5×10^8 and 5×10^9 cm⁻². Structural characterization revealed the presence of V-defects in the InGaN epilayer. Since each V-defect was associated with a TD, the structural as well as the optical properties worsened with a higher TD density in the GaN/sapphire template. It was also found that additional dislocations were generated in the *p*-GaN layer over the V-defects in the InGaN layer. Because of its superior structural quality, the peak external quantum efficiency (EQE) of the low TD density sample was three times higher than that of the high TD density sample.

© 2013 Elsevier B.V. All rights reserved.

1. Introduction

Research in III-nitrides has led to successful applications such as light emitting diodes (LEDs) and laser diodes (LDs) [1,2]. Photovoltaic utilizing these semiconductors are another potential application, where III-nitrides offer unique advantages: the band-gaps of GaN and its alloys with InN cover the entire sunlight spectrum; the direct band-gaps of InGaN alloys result in a large absorption coefficient so that a layer of a few hundred nanometers thick as the active region of the cell would suffice [3]. Furthermore, due to their strong chemical bonds, III-nitrides have a high temperature, chemical and radiation resistance [4], which is particularly advantageous for space applications. It has been predicted that multi-junction solar cells, which combine III-nitrides and other semiconductors including III-arsenides and Si, can deliver an energy conversion efficiency of over 50% [5].

Significant research progress has been made in photovoltaics based on III-nitrides. Using an InGaN/GaN double hetero-junction structure Neufeld et al. have shown a peak EQE of 60% with a flat spectral response from 370 to 410 nm [6]. The internal quantum efficiency (IQE) in a cell of similar structure was estimated at 97% through the combination of absorption and EQE measurements [7]. Using InGaN/GaN multiple quantum wells (MQWs) instead of a single InGaN epilayer allowed the incorporation of more In in the

active region without reducing quantum efficiency, extending the spectral response to 520 nm [8]. Despite all these encouraging results, there has been little work on the crystal quality of InGaN/GaN based solar cells to link the microstructure to the device performance. The present paper focuses on the effect of threading dislocations (TDs) on device performance. In particular, solar cells comprising an InGaN epilayer as the active region were fabricated from wafers with TD densities in the range of 10^8 and 10^9 cm⁻², which are typical values found for commercial nitride LEDs. The optical and electrical properties of the devices were measured and correlated with the dislocation density.

2. Experimental methods

All samples were grown in a Thomas Swan 6 × 2" close-coupled showerhead metal-organic vapor phase epitaxy (MOVPE) reactor. Trimethyl gallium (TMG), trimethyl indium (TMI), silane (50 ppm SiH₄ in hydrogen (H₂)) and bis-(cyclopentadienyl) magnesium (Cp₂Mg) and ammonia (NH₃) were used as precursors. Nitrogen (N₂) was used as the main carrier gas for InGaN growth while hydrogen (H₂) was used as the carrier gas for all other layer growth. A standard growth procedure for the GaN-on-sapphire templates was followed as outlined elsewhere [9]. The different TD density of the layers was achieved by annealing the low-temperature GaN nucleation layer in a flow of either 446 or 67 mmol/min of ammonia prior to epilayer growth, resulting in TD densities of 5×10^8 and 5×10^9 cm⁻², respectively. The TD density in the GaN template was measured by counting the pit density in AFM images after the sample surface was subjected to

* Corresponding author. Current address: Electron Microscopy Center, Swiss Federal Laboratories for Materials Testing and Research (Empa), Überlandstrasse 129, CH-8600 Dübendorf, Switzerland. Tel.: +41 766656559.

E-mail addresses: zhangyc@gmail.com, Yucheng.zhang@empa.ch (Y. Zhang).

treatment with silane and ammonia [10]. A 200 nm thick InGaN epilayer with a nominal indium content of 12% was grown using a TMI flow of 23.0 $\mu\text{mol/min}$, a TMG flow of 11.2 $\mu\text{mol/min}$ and an ammonia flow of 446 mmol/min at a susceptor temperature of 750 °C and pressure of 300 Torr. The two InGaN epilayers, labeled as LDD and HDD for the low and high TD density samples, respectively, were characterized using AFM, SEM, XRD and TEM. Two InGaN/GaN *p-i-n* hetero-structures, comprising a ca. 1 μm Si-doped *n*-type GaN layer, a 200 nm InGaN epilayer, and a 150 nm-thick Mg-doped *p*-type GaN capping layer, were grown under identical conditions as the LDD and HDD epilayer specimens described above, to form *p*-capped LDD and HDD structures. The *n*-type GaN layer was grown at 1020 °C with an electron carrier concentration of $5 \times 10^{18} \text{ cm}^{-3}$. To guarantee the integrity of the active region, a growth temperature of 900 °C was used for the *p*-type GaN layer with a hole concentration of $5 \times 10^{17} \text{ cm}^{-3}$.

The devices were fabricated using a processing routine often adopted for nitride-based LEDs: mesas of different sizes were etched using standard photo-lithography and reactive ion etching (RIE); semi-transparent Ohmic contacts to *p*-GaN were formed by thermal evaporation of Ni/Au (5/5 nm) on the mesa and subsequent rapid thermal annealing at 500 °C in air for 5 min. Contacts to *n*-GaN were formed by thermal evaporation of Al/Au (20/50 nm) and subsequent lift-off. The same metals were used for *p*-GaN contact pads.

Room temperature photoluminescence (PL) measurements were carried out using an Accent RPM2000 mapper equipped with a Q-switched 266 nm laser. Current density–voltage (*J*–*V*) characteristics were measured with a Keithley 2400 source meter. An Oriel solar simulator with a Xe lamp and AM1.5 filter was used to simulate the sunlight illumination. The EQE measurement was performed with a monochromatic illumination ranging from 370 nm to 500 nm to cover the absorption region of the InGaN epilayer. Light absorption was measured with an Agilent 8453 UV–vis spectrometer.

X-ray analysis of the LDD and HDD InGaN epilayer samples was performed using a Philips MRD high-resolution X-ray diffractometer in a triple-axis geometry. $\omega/2\theta$ scans around the 002 reflection as well as reciprocal space maps around the 004 and 105 reflections were used to determine the InGaN composition, thickness and strain-state. The samples' surface morphology was examined with atomic force microscopy (AFM) using a Veeco Dimension 3100 operated in TappingMode™ and scanning electron microscopy (SEM) on a Philips XL30. Sample cross-sections were studied with a Philips CM30 microscope and an FEI Tecnai F20 scanning transmission electron microscope (STEM). TEM samples were prepared using

a standard method: mechanical grinding and polishing down to 30 μm and then ion milling down to electron transparency using a Gatan precision ion polishing system (PIPS).

3. Results and discussion

3.1. LDD and HDD InGaN/GaN epilayers

Fig. 1 shows SEM images of the InGaN surface of the LDD and HDD samples. Individual hexagonal pits of different sizes as well as larger “trench defects” [11] can be observed on the surface of both samples. The total pit density is higher in the HDD sample at $\sim 2 \times 10^9 \text{ cm}^{-2}$ than in the LDD sample at $\sim 5 \times 10^8 \text{ cm}^{-2}$. The partial overlap of pits in the HDD sample results in an underestimate of pit density. The correlation of pit density of the InGaN epilayers with the TD density of the GaN templates as measured by AFM suggests that each pit is associated with a TD. To investigate this further, a cross-section of the two samples was studied using annular dark field (ADF) imaging in STEM (Fig. 2). The imaging condition was chosen such that the strain contrast was enhanced to reveal all the TDs [12]. TDs can be clearly observed as narrow, light-grey lines together with V-shaped pits in the InGaN epilayers. It was confirmed that each V-pit is associated with a TD at its apex. The size of the larger pits is 100 nm wide and 100 nm deep with inclined facets, presumably {10–11} planes [13]. Opening of the TDs to form V-pits occurs during the growth of the InGaN, probably to relax the strain due to the large misfit between InGaN and GaN [14]. Additionally, defects below the GaN/InGaN interface were observed. Diffraction contrast imaging from different orientations confirms that they are horizontal dislocations (HDs) rather than stacking faults (SFs). Using weak-beam dark-field (WBDF) imaging, the HDs can be observed with the reflection $g=11\text{--}20$, but not with $g=0002$, as shown in Fig. 3, indicating that the Burgers vector of the horizontal dislocations **b** also lies in the basal plane, according to the dislocation invisibility rules [15]. Because both the dislocation lines and the Burgers vector are in the basal plane, the type of the HDs cannot be determined in the cross-section sample. The HDs are located 20–100 nm below the InGaN/GaN interface, hence they are probably not misfit dislocations. We believe these dislocations are different from those misfit dislocations observed by Liu et al. which were formed due to a punch-out mechanism [16]. However, similar horizontal defects below the InGaN/GaN interface have been shown in their paper but were not discussed in detail. A different mechanism may exist to explain the formation of the HDs. However, the exact formation mechanism is as yet unknown and will require further investigations. Apart from the

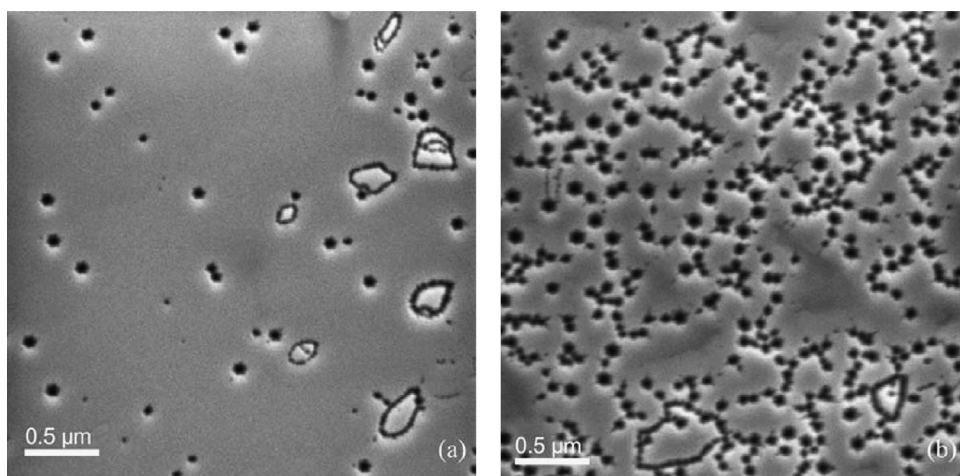


Fig. 1. SEM images showing the surface morphology of samples with (a) low dislocation density (LDD) and (b) high dislocation density (HDD).

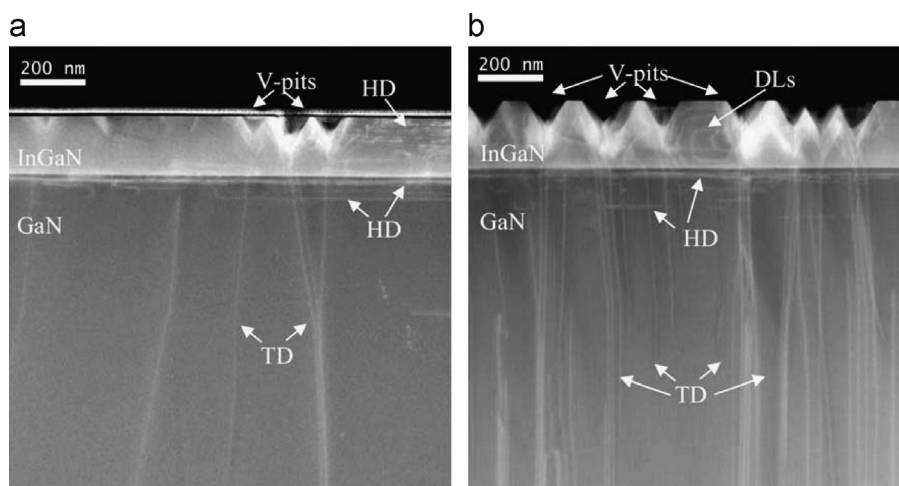


Fig. 2. STEM-ADF images of the cross-section of (a) the LDD sample and (b) the HDD sample. Note that in addition to TDs in the GaN template, there are V-pits and dislocations in the InGaN epilayer, as well as horizontal dislocations (HDs) in the GaN template near the interface. Each V-pit is associated with a TD. Dislocation loops (DLs) are visible in the InGaN.

V-defects, horizontal dislocation segments and dislocation loops (DLs) can also be observed within the InGaN epilayers (see Fig. 2).

X-ray diffraction measurements show that the indium content of the LDD sample, $12.5 \pm 1\%$, is significantly lower than that of the HDD sample, $15 \pm 1\%$. The $\omega/2\theta$ scan around the (002) reflection for the LDD sample gives a perfect fit with the simulated data (for a thickness of 192 nm) and the reciprocal space maps (RSM) taken around the 004 and 105 reflections show that the InGaN epilayer of the LDD sample is almost fully strained to the GaN template. Therefore, the horizontal dislocations in GaN below the InGaN interface as seen by TEM cannot be misfit dislocations. The much broader InGaN peak in the $\omega/2\theta$ scan of the HDD sample cannot be fitted well suggesting that the layer is inhomogeneous in strain and/or composition. Furthermore, the 004 and 105 reciprocal space maps (RSM) show that the InGaN epilayer of this sample is partially relaxed ($\sim 14\%$ relaxation). Relaxation will occur due to the high density of V-pits in this HDD sample. In addition, the indium incorporation on semi-polar facets (such as those on the V-defect) is considerably higher than that on the basal-plane [17], leading to an InGaN epilayer which is inhomogeneous in strain and/or composition for the HDD sample.

The higher structural quality of the LDD sample also results in better optical properties than those of the HDD sample. Fig. 4 shows the PL spectra from these samples in which the luminescence peaks are somewhat perturbed by thickness interference fringes. The LDD sample shows a single strong emission peak at around 425 nm, consistent with a strained InGaN epilayer with an In content of around 12% [18]. The PL peak intensity of the HDD sample is much weaker. The broad yellow band centered at around 530 nm is probably due to emission from defect states, while the weak peak at around 435 nm is assigned to InGaN near-band edge emission. The red-shift of this peak relative to that of the LDD sample is consistent with the higher indium content determined from XRD.

3.2. *p*-GaN/InGaN/n-GaN double hetero-structures

These samples have the same InGaN epilayers as the LDD and HDD specimens studied above, but with the addition of a *p*-GaN capping layer. Fig. 5 shows SEM images of the *p*-GaN surfaces before device processing, revealing hexagonal surface pits but also larger pits with a more complex shape which may relate to the trench defects seen in Fig. 1. The total pit densities are lower than

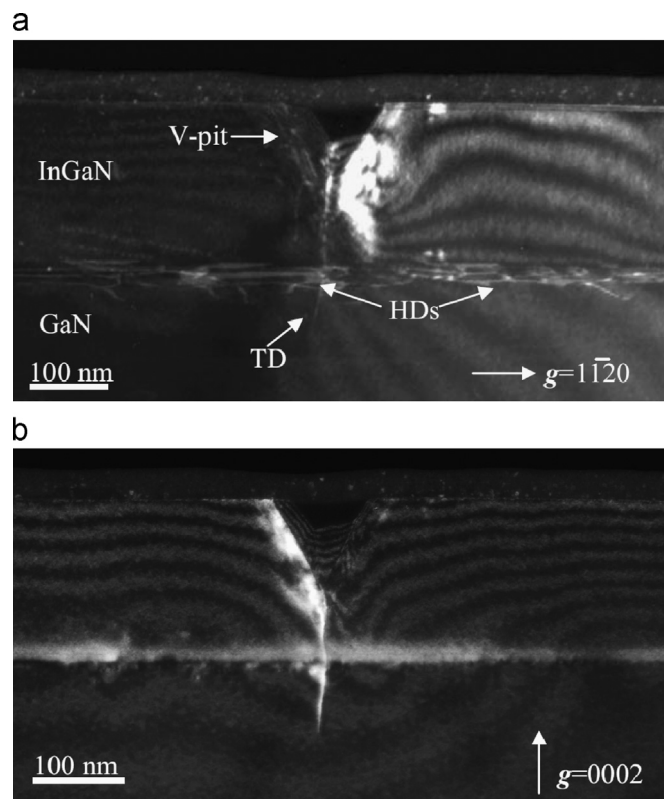


Fig. 3. WBDF images of a cross-section of the LDD sample from the same region using different reflections: (a) $g=11\bar{2}0$ and (b) $g=0002$.

those of the epilayers shown in Fig. 1, while the relative pit density ratio of ~ 10 in both samples within each batch is maintained.

Fig. 6(a) and (b) shows STEM-ADF cross-sectional images of the HDD *p*-capped sample before and after metallization. When comparing the microstructure with the HDD epilayer sample shown in Fig. 2(b), additional dislocations were generated inside the V-pits and thread up to the surface of the *p*-GaN cap. The Ni/Au and Al/Au contacts largely follow the contours of the GaN surface. Although not shown here, the LDD sample has similar features as the HDD sample but at a lower density. It appears therefore that the TDs in the GaN template open up to form V-pits in the InGaN

epilayer, which, when grown over with the *p*-type GaN contacting layer, result in additional TDs.

Light absorption of the double hetero-structures was measured before they were processed into devices (see Fig. 7). The light

absorption in both samples is nearly 80% in the wavelength range of 360–420 nm, consistent with the high absorption coefficient of InGaN. Below 360 nm, photons are absorbed by the *p*-GaN, resulting in nearly 100% absorption. The sloping absorption tail

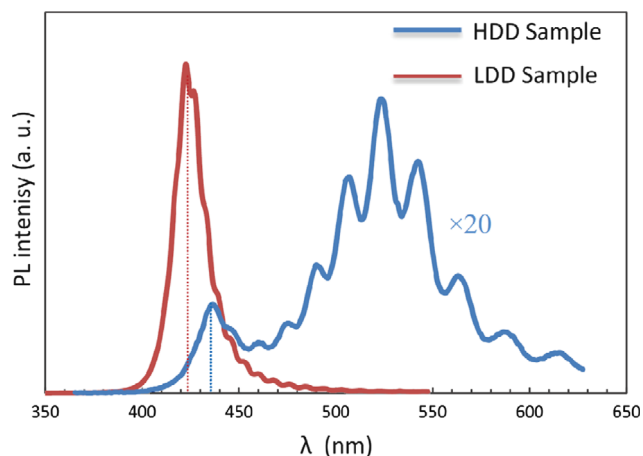


Fig. 4. PL spectra of samples. The intensity of the HDD sample is magnified 20 times.

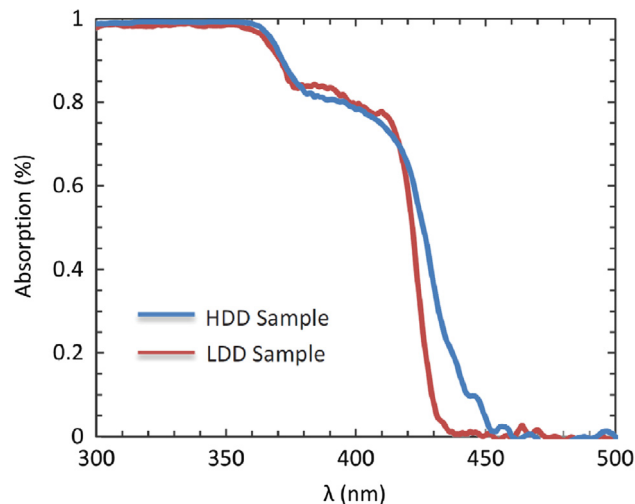


Fig. 7. Light absorption of the double hetero-structures.

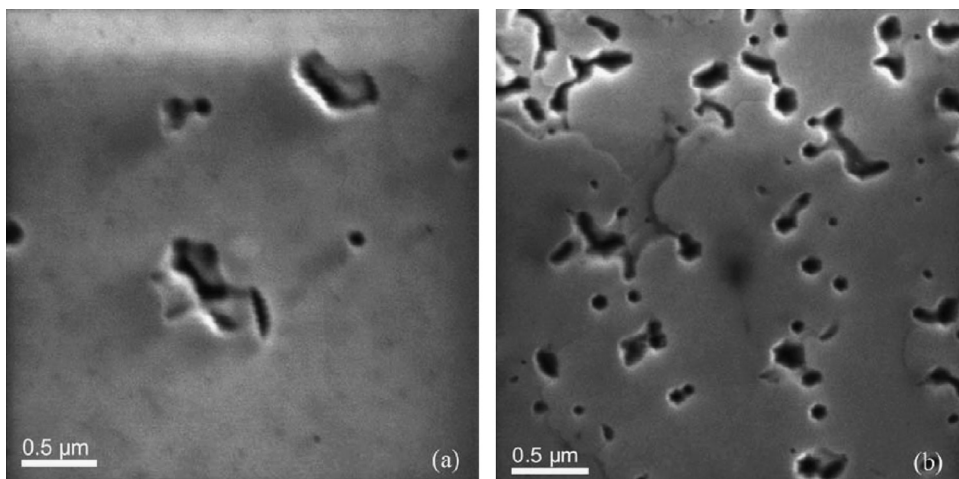


Fig. 5. SEM images show the surface morphology of the two hetero-structures: (a) LDD sample and (b) HDD sample.

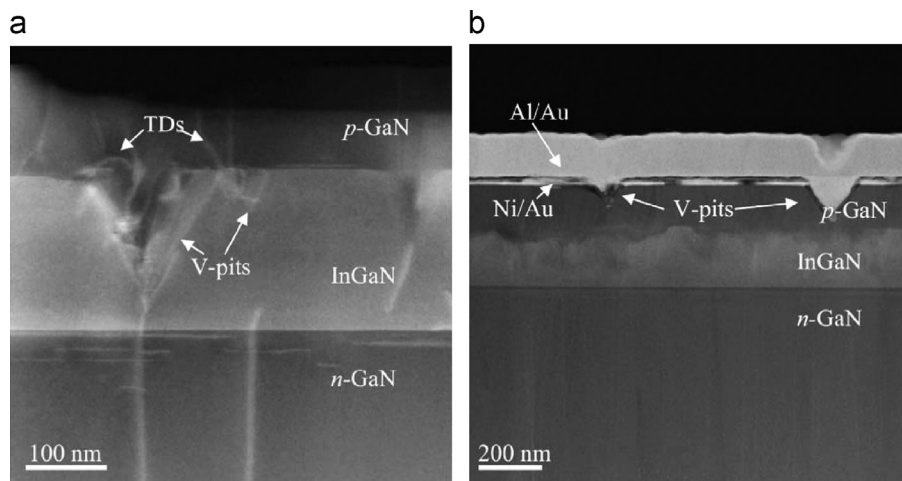


Fig. 6. (a) STEM-ADF cross-section image of the HDD sample shows additional dislocations generated inside the V-pits after the growth the *p*-GaN layer. (b) STEM-HAADF cross-section image of the HDD sample after metallization shows the V-pits in the *p*-GaN layer filled with metal.

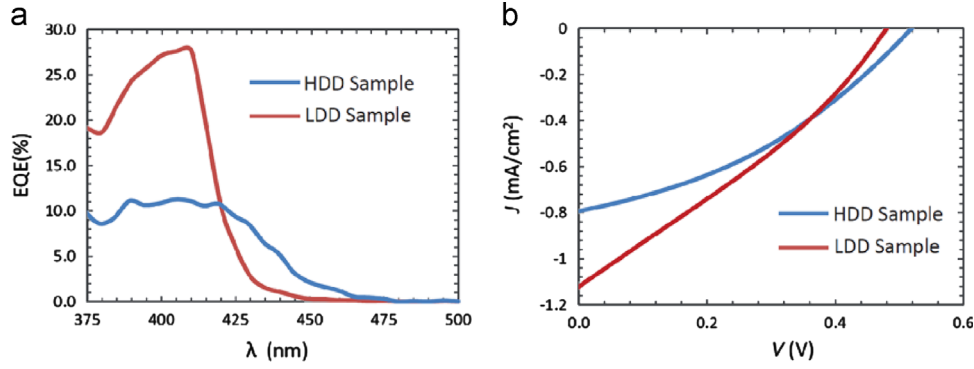


Fig. 8. (a) EQE measurement and (b) J - V curves measured under a 1.5 AM illumination condition of the device structures.

Table 1

Performance of the solar cells fabricated from the device samples. EQE_{peak} is the peak EQE, V_{oc} is the open circuit voltage, J_{sc} is the short circuit current density, FF is the fill factor, P_{max} is the maximum power extractable from the device.

	EQE_{peak} (%)	J_{sc} (mA/cm ²)	V_{oc} (V)	FF (%)	P_{max} (mW/cm ²)
LDD sample	29.8	1.12	0.48	30.2	0.162
HDD sample	11.0	0.79	0.52	38.0	0.156

at wavelengths longer than 420 nm in the HDD sample is consistent with the higher In content. It was also found that the light absorption remains the same after the thin Ni/Au (5 nm/5 nm) current spreading layer was evaporated onto the p -GaN surface.

The photovoltaic behavior of the devices was characterized by external quantum efficiency (EQE) measurements and current density versus voltage (J - V) curves measured under a 1.5 Air Mass (AM) illumination condition. As shown in Fig. 8(a), the peak EQE in the LDD sample, is almost three times higher than that in the HDD sample. At wavelengths longer than 420 nm, the EQE measured in the HDD sample is higher, mimicking the absorption profile shown in Fig. 7. Table 1 summarizes the performance of the two solar cells under a 1.5 Air Mass (AM) illumination condition. The measured short circuit current density J_{sc} for the LDD device, 1.12 mA/cm², is also higher than that for the HDD device, 0.79 mA/cm². The expected value of short circuit current density J_{sc} based on the measured EQE can be calculated using the following equation:

$$J_{sc} = \int \frac{q}{hc} S(\lambda) EQE(\lambda) \lambda d\lambda \quad (1)$$

where q is the elementary electronic charge, h is the Planck constant, c is the light speed, λ is the wavelength, $S(\lambda)$ is the 1.5 AM spectrum, and $EQE(\lambda)$ is the measured external quantum efficiency. The calculated J_{sc} is 1.90 and 1.26 mA/cm² for the LDD device and the HDD device respectively, which shows the similar trend to the measured values. When the optical absorption is taken into consideration by using the data in Fig. 7, the calculated J_{sc} is 1.35 and 0.70 mA/cm², which are reasonably consistent with the measured values of 1.12 and 0.79 mA/cm².

However, the measured open circuit voltages V_{oc} for both devices are lower than those reported in the literature [6,7]. For an ideal solar cell, the J - V curve can be modeled as:

$$J = J_{sc} - J_0 \left\{ \exp \left[\frac{q(V + Jr_s)}{kT} \right] - 1 \right\} - \frac{V + Jr_s}{r_{sh}} \quad (2)$$

where J_0 is the reverse saturation current, r_s is the series resistance, r_{sh} is the shunt resistance, k is the Boltzmann's constant and T is the temperature. The open circuit voltage V_{oc} is measured at

$J = 0$, i.e.

$$J_{sc} = J_0 \left[\exp \left(\frac{qV_{oc}}{kT} \right) - 1 \right] + \frac{V_{oc}}{r_{sh}} \quad (3)$$

Hence V_{oc} decreases with a decreasing J_{sc} , a decreasing r_{sh} , and an increasing J_0 which can be expressed as:

$$J_0 = q \left(\sqrt{\frac{D_p}{\tau_p}} \frac{n_i^2}{N_D} + \sqrt{\frac{D_n}{\tau_n}} \frac{n_i^2}{N_A} \right) \quad (4)$$

where $D_{n,p}$ and $\tau_{n,p}$ are the diffusion coefficients and the carrier life times of holes and electrons respectively; $N_{D,A}$ are the donor and acceptor concentrations at the n - and p -side respectively; n_i is the intrinsic carrier density. The presence of the observed defects inside the V-pits may reduce the carrier life $\tau_{n,p}$, hence increases J_0 , leading to the reduced V_{oc} . Additionally, the V-pits may act as current leakage paths such that r_{sh} and hence V_{oc} is reduced. However, it is noticed that the open circuit voltage V_{oc} and the fill factor FF of the LDD device are slightly lower than those of the HDD device. Fig. 8(b) indicates a smaller shunt resistance in the LDD device. It is not yet clear why the LDD device, which has a better crystal quality and a larger J_{sc} , possesses the unexpected smaller r_{sh} . It may be due to the fact that the leakage path has already been saturated with the high density of V-pits. Additionally it cannot be ruled out that the device processing is not optimized for the LDD samples. Further investigation is required to understand the phenomenon. The maximum power that can be delivered, P_{max} , is slightly higher for the LDD device than the HDD device.

While both samples show a photovoltaic behavior, it is clear that the external quantum efficiency is affected by the TD density in the template, as the LDD sample shows a nearly three-fold higher peak EQE than the HDD sample, which leads to a higher J_{sc} . However, due to the conditions adopted to grow the thick InGaIn epilayers, TDs were opened up to form V-defects in the active region. The facets of the V-defects are probably relaxed and have a large lattice mismatch with GaN grown on the top. Consequently, the growth of the capping layer introduces in the active region more dislocations, as shown in Fig. 6, which may act as recombination centers [19] or become charged cores [20] to hinder photon-induced carriers from being collected. The presence of V-defects in the p -GaIn layer can also act as leakage paths owing to the contact metals filling the defects during device processing, which also reduces V_{oc} . Our future work will try to optimize the growth of InGaIn layers to prevent the formation of V-pits associated with TDs. This may be accomplished through a better designed structure for the active region such as multiple quantum wells (MQWs).

4. Conclusion

We have compared working solar cells with a high and a low dislocation density, based on an InGaN/GaN $p-i-n$ double hetero-junction. We have shown that structural defects in the material have a significant effect on the performance of the cells. In particular, a high density of V-pits was formed in the InGaN epilayer which originate from TDs in the GaN/sapphire template. The V-defects introduce additional TDs in the p -GaN capping layer that are detrimental to the performance of the devices. V-pits in the p -GaN capping layer can act as a leakage path when filled with contact metals. Further improvement in the performance of InGaN/GaN solar cells should result from an optimized InGaN epilayer free of V-pits.

Acknowledgment

The author Y. Zhang would like to thank Engineering and Physical Sciences Research Council (EPSRC) UK, Science Bridge Award scheme for financial support.

References

- [1] C.J. Humphreys, Solid state lighting, *MRS Bulletin* 33 (2008) 459–470.
- [2] S. Nakamura, G. Fasol, *The Blue Laser Diode*, Springer, Berlin, 2000.
- [3] J.F. Muth, J.H. Lee, I.K. Shmagin, R.M. Kolbas, H.C. Casey, B.P. Keller, U.K. Mishra, S.P. DenBaars, Absorption coefficient, energy gap, exciton binding energy, and recombination lifetime of GaN obtained from transmission measurements, *Applied Physics Letters* 71 (1997) 2572–2574.
- [4] J. Wu, W. Walukiewicz, K.M. Yu, W. Shan, J.W. Ager, E.E. Haller, H. Lu, W.J. Schaff, W.K. Metzger, S. Kurtz, Superior radiation resistance of $\text{In}_{1-x}\text{Ga}_x\text{N}$ alloys: full-solar spectrum photovoltaic material system, *Journal of Applied Physics* 94 (2003) 6477–6482.
- [5] D.J. Friedman, Progress and challenges for next-generation high-efficiency multi-junction solar cells, *Current Opinion in Solid State and Materials Science* 14 (2010) 131–138.
- [6] C.J. Neufeld, N.G. Toledo, S.C. Cruz, M. Iza, S.P. DenBaars, U.K. Mishra, High quantum efficiency InGaN/GaN solar cells with 2.95 eV band gap, *Applied Physics Letters* 93 (2008) 143502–1–143502–3.
- [7] E. Matioli, C.J. Neufeld, M. Iza, S.C. Cruz, A.A. Al-Heji, X. Chen, R.M. Farrell, S. Keller, S.P. DenBaars, U.K. Mishra, S. Nakamura, J. Speck, C. Weisbuch, High internal and external quantum efficiency InGaN/GaN solar cells, *Applied Physics Letters* 98 (2011) 021102.
- [8] R.M. Farrell, C.J. Neufeld, S.C. Cruz, J.R. Lang, M. Iza, S. Keller, S. Nakamura, S.P. DenBaars, U.K. Mishra, J. Speck, High quantum efficiency InGaN/GaN multiple quantum well solar cells with spectral response extending out to 520 nm, *Applied Physics Letters* 98 (2011) 201107–1–201107–3.
- [9] R. Datta, M.J. Kappers, M.E. Vickers, J.S. Barnard, C.J. Humphreys, Growth and characterization of GaN with reduced dislocation density, *Superlattices and Microstructures* 36 (2004) 393–401.
- [10] R.A. Oliver, M.J. Kappers, J. Sumner, R. Datta, C.J. Humphreys, Highlighting threading dislocations in MOVPE-grown GaN using an in situ treatment with SiH_4 and NH_3 , *Journal of Crystal Growth* 289 (2006) 506–514.
- [11] F.C.P. Massabau, S.L. Sahonta, L. Trinh-Xuan, S. Rhode, T.J. Puchler, M.J. Kappers, C.J. Humphreys, Morphological, structural, and emission characterization of trench defects in InGaN/GaN quantum well structures, *Applied Physics Letters* 101 (2012) 212107–1–212107–3.
- [12] J.M. Cowley, Scanning-transmission electron microscopy of thin specimens, *Ultramicroscopy* 2 (1976) 3–16.
- [13] X.H. Wu, C.R. Elsass, A. Abare, M. Mack, S. Keller, P.M. Petroff, S.P. DenBaars, J.S. Speck, S.J. Rosner, Structural origin of V-defects and correlation with localized excitonic centers in InGaN/GaN multiple quantum wells, *Applied Physics Letters* 72 (1998) 692–694.
- [14] I.H. Kim, H.S. Park, Y.J. Park, T. Kim, Formation of V-shaped pits in InGaN/GaN multiquantum wells and bulk InGaN films, *Applied Physics Letters* 73 (1998) 1634–1636.
- [15] P.B. Hirsch, A. Howie, R.B. Nicholson, *Electron Microscopy of Thin Crystals*, Huntington, Krieger, New York, 1977.
- [16] R. Liu, J. Mei, S. Srinivasan, F.A. Ponce, H. Omiya, Y. Narukawa, T. Mukai, Generation of misfit dislocations by basal-plane slip in InGaN/GaN heterostructures, *Applied Physics Letters* 89 (2006) 201911–1–201911–3.
- [17] M.J. Kappers, J.L. Hollander, C. McAleese, C.F. Johnston, R.F. Broom, J.S. Barnard, M.E. Vickers, C.J. Humphreys, Growth and characterisation of semi-polar (11–22) InGaN/GaN MQW structures, *Journal of Crystal Growth* 300 (2007) 155–159.
- [18] J. Wu, When group-III nitrides go infrared: new properties and perspectives, *Journal of Applied Physics* 106 (2009) 011101–1–011101–28.
- [19] S.J. Rosner, E.C. Carr, M.J. Ludowise, G. Girolami, H.I. Erikson, Correlation of cathodoluminescence inhomogeneity with microstructural defects in epitaxial GaN grown by metalorganic chemical-vapor deposition, *Applied Physics Letters* 70 (1997) 420–422.
- [20] D. Cherns, C. Jiao, Electron holography studies of the charge on dislocations in GaN, *Physical Review Letters* 87 (2001) 205504–1–205504–4.